Excitonic approach to the ultrafast optical response of semiconductor quantum wells

Dawei Wang and Marc M. Dignam*
Department of Physics, Queen's University, Kingston, Ontario, Canada K7L 3N6
(Received 22 December 2008; revised manuscript received 26 March 2009; published 28 April 2009)

We use a basis of bound and unbound excitons to study the coherent dynamics of optically excited excitons in a semiconductor quantum well. We derive a set of excitonic dynamic equations for quantum wells that includes the influence of phase-space filling and the exchange interaction. We calculate the nonlinear absorption for excitation by a short pulse resonant on the 1*s* exciton, and show that the 1*s* excitonic peak is reduced and blueshifted as the exciton density increases. By examining the dynamics of the populations in the different excitonic states, we show that at moderate densities ($n=1.3\times10^{10}$ cm^{-2}) the absorption near the 1*s* peak is well described using only the 1*s* excitonic state but that at higher densities ($n=5.0\times10^{10}$ cm^{-2}) the other excitons—both optically active and optically inactive—play a significant role. For moderate densities, we derive analytical expressions to describe the density-dependent blueshift and bleaching of the 1*s* excitonic resonance. Finally, we discuss the potential advantages of this formalism for the investigation of both interband and intraband dynamics in quantum wells.

DOI: 10.1103/PhysRevB.79.165320 PACS number(s): 78.47.−p, 42.65.Re, 73.21.Cd, 78.67.Pt

I. INTRODUCTION

The nonlinear optical response of a quantum well (QW) has been studied for many years.[1–9] However, the many-body dynamics of this important system has not generally been modeled using a strictly excitonic approach, despite the fact that the excitonic signature dominates its optical response. In addition, with the advance of ultrafast laser and terahertz (THz) technologies, the study of intraexcitonic transitions induced by THz pulses in semiconductor nanostructures have attracted much attention. Intraexcitonic spectroscopy has emerged as a powerful tool in investigating the low-energy resonances and dynamics of excitons in semiconductor nanostructures.[10–12] However, there is no general theory that allows one to model or simulate the effects of *excitonic* dynamics on this intraband dynamic process. In this paper, we apply the recently developed excitonic dynamic equations (EXEs) (Ref. 13) to calculate the nonlinear absorption spectra and exciton population dynamics in a quantum well in the presence of phase-space filling (PSF) and the exchange interaction.

Over the years, many theoretical approaches have been developed to study the nonlinear optical response of semiconductors. Nonequilibrium Green's function and density-matrix techniques are among the most commonly used methods.[14] The well-known semiconductor Bloch equations (SBEs) are based on the second approach,[15] as are the dynamics controlled truncation (DCT) equations.[16] These are powerful theoretical approaches that have been used to study many optical phenomena in semiconductors. While many of these approaches use an electron-hole basis, another somewhat less common practice is to employ an excitonic basis. At low to moderate densities, when the semiconductor is excited resonantly near the 1*s* excitonic peak, an excitonic approach can simplify the treatment of the nonlinear optical response, particularly at short times when bound excitons dominate. Because the bound excitons form a discrete basis, the number of required basis functions can be greatly reduced relative to an electron-hole approach. Excitonic approaches are also used to investigate the possible realization of exciton Bose-Einstein condensation.[17,18]

Although there are a number of different approaches that examine exciton-like carrier correlations using an electron-hole basis or a combination of electron-hole and excitonic bases,[19,20] there are relatively few purely excitonic approaches to this problem. By an excitonic approach, we refer to any approach that models the response of the system using only excitonic operators. One obvious difficulty that arises in developing an excitonic approach is that, unless one imposes a specific pairing scheme, the mapping of the electron-hole basis onto the excitonic basis is not one-to-one. For example, when one has a set of four uncorrelated particles consisting of two electrons and two holes in definite single-particle states, there are still two different ways in which these particles could be paired even if we exclude the possibility of pairing like particles (electron with electron and hole with hole). There are two basic approaches to the pairing when the Coulomb interaction is also included. The first is to restrict the electron-hole pair to a fixed internal state (the 1*s* state in most cases) but to allow the center-of-mass (COM) momenta of the pair to take any value.[21,22] The second approach is to pair electrons and holes that have opposite momenta;[13] this then allows for excitons with any internal state ($1s,2s,2p\ldots$ including continuum exciton states) but restricts the basis to excitons with zero COM momenta. Trying to use both schemes simultaneously will lead to the problem that the mapping will no longer be one-to-one. These two approaches have different strengths and weaknesses. The first approach requires resonant excitation of 1*s* excitons and cannot account for THz-induced transitions between the internal excitonic states (e.g., 1*s* to 2*p*). However, it allows one to model four-wave mixing experiments and to examine the time evolution of the distribution of the exciton momenta, including the coherent scattering of the excitons to optically inactive excitonic states with nonzero COM momenta.[22] It also can account for the formation of biexcitons at some level.[21] The second approach, which is the approach that we adopt in this paper, does not account for any scattering of excitons out of the light cone and cannot account for the

formation of biexcitons. Also, because it requires all excitons to have the same COM momenta, it cannot be used to model four-wave mixing experiments. However, because it includes all internal states, it allows for excitation of states other than the 1*s* state. Thus, it can model the response of the system to a terahertz field that induces transitions between excitonic internal states while retaining the potentially important PSF and exchange effects. In addition, it accounts for coherent scattering of the optically active *s*-symmetry excitonic states into optically inactive excitonic states $(2p,3p,3d\ldots)$.[13,23]

One of the key challenges in an excitonic approach is how to deal with the PSF effects associated with the composite nature of excitons. These effects results in non-Bosonic density-dependent commutation relation for the excitonic operators. There are essentially three ways of dealing with this. The first is to assume that the density is low enough such that PSF effects are negligible. This approach has been used by many authors,[22,24,25] and at moderate excitation densities is a reasonable approximation. The second is to "bosonize" the excitons; this results in the definition of creation and annihilation operators that obey strict Boson commutation relations.[26,27] There is still some controversy regarding bosonization schemes; for example, Combescott and Beebeder-Matibet[28] have shown that it is not possible to derive an effective Hamiltonian for these Bosons beyond the two-exciton regime if only four-operator interactions are included. The third approach, which is the approach that we adopt here, is to use the density-independent non-Bosonic exciton creation and annihilation operators, and to explicitly take into account their exact density-dependent commutation relations.[13,24,29,30]

We employ an excitonic approach that includes both PSF and exchange to study the exciton dynamics in a QW excited by a single short optical pulse resonant near the band edge. We have presented this approach in its most general form in a previous work[13] and compared it to the SBEs for a simple model of a quantum wire. One distinct feature of this excitonic approach is that it treats the intraband dynamics as transitions between different exciton states and that the intraband coherence functions are kept unfactorized, which increases the accuracy of the results. In a recent paper, we have also employed this approach (in the linear regime) to model the tunable THz gain from biased semiconductor superlattices (BSSLs).[31] The central problem we pursue in this paper is the ultrafast dynamics of excitons and their influence on the ultrafast nonlinear absorption in QWs. For this purpose, we focus on the dynamics in the coherent regime when most of the excitons are still in $\boldsymbol{K}=0$ COM momentum state. This makes possible the use of our approach that includes only $\boldsymbol{K}=0$ excitons.

In this paper, we derive the excitonic dynamic equations for a QW from the general excitonic equations of Ref. 13. We then present numerical results for the nonlinear absorption spectra for both moderate and relatively high intensity pulses. We also present the time evolution of the populations in the various excitonic states to aid in the understanding the effects of PSF and exchange on the absorption. We propose a number of possible approximations to increase the computation efficiency of the EXEs; these approximations are motivated by the fact that, depending on the excitation condition, only a subset of the exciton states play a significant role in the absorption spectra. We show that, for resonant excitation of the 1*s* exciton state at moderate carrier densities ($\sim 1.3 \times 10^{10}$ cm^{-2}), a basis consisting of only the 1*s* exciton state is sufficient. However, for higher densities ($\sim 5.0 \times 10^{10}$ cm^{-2}), the blueshift of the 1*s* peak and redshift of the band-edge absorption can only be accurately described if higher-energy optically inactive excitonic states are included in the calculation.

In addition to providing a computational tool for the numerical simulation of nonlinear dynamics in a QW, a second aim of this paper is to exploit the excitonic approach to gain insight into the nonlinear optical response of a QW. In particular, we examine the relation between the population dynamics, and the blueshift and bleaching (the reduction in the oscillator strength) of the 1*s* excitonic resonance that have been observed.[1,3,8] In the 1980s, Schmitt-Rink *et al.*[2] considered the influence of phase-space filling and the exchange interaction on the exciton resonance and the oscillator strength by analyzing exciton wave functions. The SBE approach was also used to investigate this phenomena,[5,8,32] where temperature effects can be included.[5] In a recent study of the absorption and emission of exciton-polariton modes, the retarded Green's function approach takes into account propagation effects.[9] In this paper, however, we apply the excitonic approach to understand the influence of the various excitonic populations on the optical response of a QW. An important feature is that it clearly connects the exciton (as opposed to free-carrier) population dynamics to the optical response. We use this property to obtain *analytic* expressions for the blueshift and bleaching of the 1*s* excitonic peak. We also briefly discuss how this excitonic approach can be used to understand the effect of the exciton dynamics on the response to a terahertz field, which is of much interest in recent years.[12,33]

This paper is organized as follows. We first introduce the general EXEs in Sec. II. We then examine how to adapt the general EXEs to the particular case of a QW in Sec. III. In Sec. IV, we present numerical results for the nonlinear absorption and the exciton population dynamics for moderate-intensity excitation of the QW. We then discuss potential approximations that can increase the efficiency of the EXEs in Sec. V. In Sec. VI, we present analytical expressions obtained using the EXEs for the blueshift and bleaching of the 1*s* excitonic peak. In Sec. VII we examine the response of a higher-intensity pulse to examine the effects of the higher-energy bound and unbound excitons on the nonlinear response. Finally, in Sec. VIII, we present our conclusions.

II. GENERAL EXCITONIC DYNAMIC EQUATIONS AND EXCITONIC COEFFICIENTS

The general EXEs for semiconductor nanostructures have been obtained and explained in our previous work.[13] We include a brief description of them and their derivation here for completeness and for later reference in this paper.

We derive the EXEs by first transforming the Hamiltonian for a photoexcited semiconductor system in Fermion space[15] to obtain the Hamiltonian H in the quasiboson (qboson) pair

space using the Usui transformation.[29] The qboson states are electron-hole pair states where the electron and hole are in single-particle eigenstates of the semiconductor nanostructure with the pairing chosen such that the total momentum is zero. Thus, in a quantum well, the envelope function for a qboson state takes the form

$$\chi_{\boldsymbol{p}}(\boldsymbol{r},z_e,z_h)=f_e(z_e)f_h(z_h)\frac{\exp(i\boldsymbol{p}\cdot\boldsymbol{r})}{\sqrt{A}}, \tag{1}$$

where A is the in-plane area, $\boldsymbol{p}(-\boldsymbol{p})$ is the in-plane wave vector for the electron (hole), $\boldsymbol{r}=\boldsymbol{r}_e-\boldsymbol{r}_h$ is the electron-hole separation in the plane of the quantum well, and $f_e(z_e)$ and $f_h(z_h)$ are the electron and hole envelope functions for the lowest energy quantum well states in the z direction. We take $B_{\boldsymbol{p}}^{\dagger}$ to be the creation operator for such a qboson pair. We then use the Heisenberg equation of motion, the (non-Bosonic) commutation relations for the $B_{\boldsymbol{p}}^{\dagger}$ and $B_{\boldsymbol{q}}$, and the qboson Hamiltonian to obtain the dynamic equations for the qboson operators $B_{\boldsymbol{p}}^{\dagger}$ and $B_{\boldsymbol{p}}^{\dagger}B_{\boldsymbol{q}}$.

The true excitonic states (eigenstates of the Hamiltonian with only one electron and one hole) with energy E_μ can be expressed as

$$\Phi_\mu(\boldsymbol{r},z_e,z_h)=\sum_{\boldsymbol{p}} c_\mu^{\boldsymbol{p}}\chi_{\boldsymbol{p}}(\boldsymbol{r},z_e,z_h), \tag{2}$$

where $c_\mu^{\boldsymbol{p}}$ are the expansion coefficients. Similarly, the creation operator for such a true excitonic state is given by the canonical transformation

$$B_\mu^{\dagger}=\sum_{\boldsymbol{p}} c_\mu^{\boldsymbol{p}}B_{\boldsymbol{p}}^{\dagger}. \tag{3}$$

We note that these true excitons are not bosons and thus the operators do not obey the Boson commutation relations except in the limit of zero density (see, e.g., Ref. 29). Finally, we use Eq. (3) to transform the qboson dynamic equations into the dynamic equations for the true excitons. Two sets of dynamic equations are obtained after factorization is applied.[13] The factorization is essentially the same as is used in deriving the SBEs except that we do not factor the intraband coherence functions into products of interband coherence functions.[13] We note that, because we are allowing only exciton states with zero center-of-mass momentum, our approach includes only the exchange interaction between excitons.[13] However, for the system being considered, it has been shown that this is the dominant interaction.[34]

The first set of equations is for the interband coherence functions,

$$\begin{aligned}
&i\hbar\frac{d}{dt}\langle B_\mu^{\dagger}\rangle+E_\mu\langle B_\mu^{\dagger}\rangle\\
&\quad=-i\hbar\frac{\langle B_\mu^{\dagger}\rangle}{T_{\text{inter}}}+2\sum_{\mu_1,\mu_2,\mu_3}R^{\mu}_{\mu_1,\mu_2,\mu_3}\langle B_{\mu_1}^{\dagger}\rangle\langle B_{\mu_2}^{\dagger}B_{\mu_3}\rangle\\
&\qquad+\mathcal{E}(t)\cdot\boldsymbol{M}_{cv}^{*}\Big(C_\mu-2\sum_{\mu_1,\mu_2}C_{\mu,\mu_1,\mu_2}\langle B_{\mu_1}^{\dagger}B_{\mu_2}\rangle\Big).
\end{aligned} \tag{4}$$

The second set of dynamic equation is for the intraband coherence functions,

$$\begin{aligned}
&i\hbar\frac{d}{dt}\langle B_\mu^{\dagger}B_\nu\rangle+(E_\mu-E_\nu)\langle B_\mu^{\dagger}B_\nu\rangle\\
&\quad=-i\hbar\langle B_\mu^{\dagger}B_\nu\rangle\left[\frac{1}{T_{\text{intra}}}+\delta_{\mu,\nu}\left(\frac{1}{T_{\text{decay}}}-\frac{1}{T_{\text{intra}}}\right)\right]\\
&\qquad+2\sum_{\mu_1,\mu_2,\mu_3,\mu_4}Z^{\mu,\nu}_{\mu_1,\mu_2,\mu_3,\mu_4}\langle B_{\mu_1}^{\dagger}B_{\mu_4}\rangle\langle B_{\mu_2}^{\dagger}B_{\mu_3}\rangle\\
&\qquad+[\mathcal{E}(t)\cdot\boldsymbol{M}_{cv}^{*}C_\mu\langle B_\nu\rangle-\mathcal{E}^{*}(t)\cdot\boldsymbol{M}_{cv}C_\nu^{*}\langle B_{\boldsymbol{\mu}}^{\dagger}\rangle]\\
&\qquad-2\sum_{\mu_1,\mu_2,\mu_3}[\mathcal{E}(t)\cdot\boldsymbol{M}_{cv}^{*}U^{\mu,\nu}_{\mu_1,\mu_2,\mu_3}\langle B_{\mu_1}^{\dagger}B_{\mu_2}\rangle\langle B_{\mu_3}\rangle\\
&\qquad-\mathcal{E}(t)\cdot\boldsymbol{M}_{cv}U^{\nu,\mu*}_{\mu_3,\mu_2,\mu_1}\langle B_{\mu_1}^{\dagger}\rangle\langle B_{\mu_2}^{\dagger}B_{\mu_3}\rangle].
\end{aligned} \tag{5}$$

In Eq. (4), T_{inter} is the phenomenological interband dephasing time constant for $\langle B_\mu^{\dagger}\rangle$ while in Eq. (5), T_{intra} is the intraband dephasing time constant for $\langle B_\mu^{\dagger}B_\nu\rangle$ (where $\mu\neq\nu$) and T_{decay} is the decay constant for the exciton populations $\langle B_\mu^{\dagger}B_\mu\rangle$. In both equations, $\mathcal{E}(t)$ is the electric field of the exciting optical pulse, and $\boldsymbol{M}_{cv}$ is the dipole moment between the conduction and valence bands in the quantum well at $\boldsymbol{k}=0$. The coefficients, $R^{\mu}_{\mu_1,\mu_2,\mu_3}$, C_μ, C_{μ,μ_1,μ_2}, $Z^{\mu,\nu}_{\mu_1,\mu_2,\mu_3,\mu_4}$, and $U^{\mu,\nu}_{\mu_3,\mu_2,\mu_1}$ are *excitonic coefficients* (XCs) that are responsible for phase-space filling and exchange effects.[13] Their net effects will determine the optical response from a semiconductor nanostructure. They are defined and discussed in more detail in Appendix A. Although it is straight forward to derive the commutation relations for the true excitonic operators, the above dynamic equations cannot be derived from these commutation relations alone, as the commutation relations do not explicitly contain the fact that $B_{\boldsymbol{p}}^{\dagger}B_{\boldsymbol{p}}^{\dagger}=0$.

The above two dynamic equations [Eqs. (4) and (5)] can be solved numerically to obtain $\langle B_\mu^{\dagger}\rangle$ and $\langle B_\mu^{\dagger}B_\nu\rangle$, which can then be used to calculate the interband and intraband polarizations and the exciton population of the system that is investigated.[13]

The dynamic equations can be used in numerical simulations as well as in deriving analytical expressions. We will present the results of numerical simulations in Sec. IV and in Sec. VI, will use these expressions to derive analytical expressions for the blueshift and bleaching of the 1s excitonic absorption peak.

III. EXCITONIC DYNAMIC EQUATIONS AND THE QUANTUM WELL MODEL

In our previous work we studied the exciton dynamics in a one-dimensional (1D) model of a quantum wire.[13] Applying these equations to the study of the exciton dynamics in a QW is computationally more difficult as we now need two indices to label an exciton state. Thus, all things being equal, we would expect that more coherence functions will be required. In particular, the number of required intraband coherence functions, $\langle B_\mu^{\dagger}B_\nu\rangle$, could become huge. Thus, we need an efficient way to organize exciton states and simplify the dynamic equations; this is the focus of this section.

In this paper, we will sometimes examine the exciton states in a strict two-dimensional (2D) system (an infinitely large 2D system with no thickness) for comparison and to

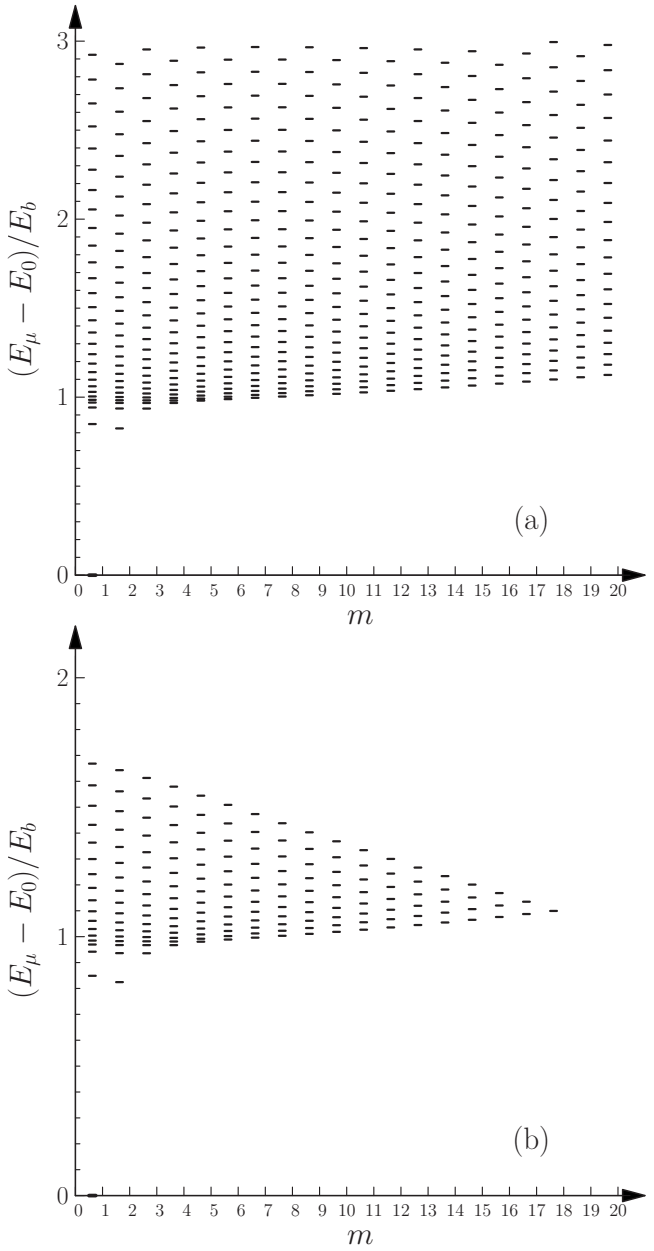

FIG. 1. Energy levels of (a) exciton states and (b) the exciton states included in our full simulation. Note the $1s$ level is $E_\mu = E_0$.

obtain analytic results. In a strict 2D system, the exciton energy for bound states only depends on the principle quantum number, n, and for each n, there are $2n+1$ exciton states with angular momentum $m\hbar$ where $|m| \leq n$.[15,23] However, the energy of an exciton in a QW is not solely determined by n. This is demonstrated in Fig. 1(a), where we plot the exciton energies for different n and m. Thus, in a QW, a good way to organize exciton states is to choose the angular momentum, m, as the major index. Then, for each angular momentum m, there are an infinite number of energy levels. In performing numerical computations, we specify the maximum angular momentum, $m_{\max}$, of the states employed and number of exciton states, n_m, included for each angular momentum m.

A simple calculation shows that, for a strict 2D system, if we keep the exciton energy level up to $n=N$, then we have N^2 exciton states, and thus N^2 interband coherence functions and N^4 intraband coherence functions. The exact number of exciton states for a QW with energies less than a given value is not simply N^2 but can also be quite large to obtain converged results [see Fig. 1(a)]. Thus it is important to use symmetry to reduce the number of coherence functions needed. There are two key symmetries that can be exploited: rotational symmetry and mirror symmetry in the plane.

A significant reduction in the required number of coherence functions can be achieved by considering the rotational symmetry of the QW. Using this symmetry, we find that $\langle B^\dagger_{(n_1,m_1)}\rangle = 0$ if $m_1 \neq 0$, i.e., there is no interband coherence except for s exciton states. We also find that $\langle B^\dagger_{(n_1,m_1)} B_{(n_2,m_2)}\rangle = 0$ if $m_1 \neq m_2$, i.e., there is no intraband coherence between excitonic states having different angular momentum. Thus in our dynamic equations, only intraband coherence functions of the form $\langle B^\dagger_{(n_1,m)} B_{(n_2,m)}\rangle$ survive.

A further reduction in the number of required intraband coherence functions can be made by considering the mirror symmetry of the QW. We find that this symmetry results in the identity, $\langle B^\dagger_{(n_1,m)} B_{(n_2,m)}\rangle = \langle B^\dagger_{(n_1,-m)} B_{(n_2,-m)}\rangle$.

Thus, the above two symmetries result in the following three relations:

$$\langle B^\dagger_{\mu_1}\rangle = 0, \quad \text{for} \quad m_1 \neq 0, \tag{6}$$

$$\langle B^\dagger_{\mu_1} B_{\mu_2}\rangle = 0, \quad \text{for} \quad m_1 \neq m_2, \tag{7}$$

$$\langle B^\dagger_{(n_1,m_1)} B_{(n_2,m_1)}\rangle = \langle B^\dagger_{(n_1,-m_1)} B_{(n_2,-m_1)}\rangle, \tag{8}$$

where $\mu_i = (n_i, m_i)$, $i = 1, 2$. These relations have been verified directly in our numerical simulations, and can also be proved by analyzing the EXEs and XCs directly.[23]

With the three relations in Eqs. (6)–(8), we only need to include the following terms in our EXEs: the interband coherence terms $\langle B^\dagger_{(n,0)}\rangle$, the intraband coherence terms (including population) $\langle B^\dagger_{(n_1,m_1)} B_{(n_2,m_1)}\rangle$ where $m_1 \geq 0$, and the intraband coherence terms $\langle B^\dagger_{(n_1,m_1)} B_{(n_2,m_1)}\rangle$ where $n_1 \geq n_2$ because $\langle B^\dagger_{(n_1,m_1)} B_{(n_2,m_1)}\rangle = \langle B^\dagger_{(n_2,m_1)} B_{(n_1,m_1)}\rangle^*$.

In this paper, we present numerical results obtained using the EXEs for a 67 Å $Ga_{0.7}Al_{0.3}As$ QW that is excited using a short optical pulse centered on the $1s$ excitonic resonance. We present the calculated nonlinear absorption spectra as well as the time evolution of the total exciton density and the exciton population distribution among excitonic states (Secs. IV, V, and VII).

We employ a model that includes the lowest heavy-hole and electron subbands in the parabolic approximation. The system parameters used, such as the band offsets and the effective masses, are given in Refs. 35–37. Using these parameters, the in-plane excitonic Bohr radius is found to be $r_B \simeq 157$ Å. We excite the QW using a Gaussian optical pulse with an electric field given by

$$\mathcal{E}(t) = \boldsymbol{E}_0 e^{-i\omega_c t - t^2/\tau_p^2} + \text{c.c.}, \tag{9}$$

where ω_c is the central frequency of the optical pulse, which is chosen to be in resonance with the $1s$ exciton state. In the

following plots, the energy unit we use is the binding energy of the $1s$ exciton in the QW, which is found to be $E_b = 2.49R_y = 9.15$ meV, and unit of time is taken to be $\tau_0 = \hbar/R_y = 179.4$ fs, where $R_y = 3.67$ meV is the exciton Rydberg. In all sections except Sec. VII, the pulse length is taken to be $\tau_p = 1.6\tau_0 = 287.0$ fs. This length is chosen to be long enough such that only $1s$ excitons are excited directly but also short enough to be much less than the dephasing times. In Sec. VII, we consider a shorter pulse with $\tau_p = 107.6$ fs so as to directly excite some unbound carriers as well.

For the computation of the nonlinear absorption, the interband and intraband dephasing times are $T_{\text{inter}} = 3.2\tau_0$, and $T_{\text{intra}} = 1.5T_{\text{inter}}$, respectively, and the population decay time of $T_{\text{decay}} = T_{\text{intra}}$. For the computation of the time evolution of the exciton populations, we use $T_{\text{inter}} = T_{\text{intra}} = T_{\text{decay}} = \infty$. This is done so that the effects of PSF, and exchange on the population dynamics can be clearly separated from decay and dephasing effects. We have discussed the general effects of choosing different time constants in Ref. 13.

In Fig. 1(a) we plot a large number of excitonic energy levels for different m for the QW. In Fig. 1(b) we show only the states that are included in our *full simulation*. This particular choice of states was made by considering an ideal 2D system, where a highest energy level with $m=0$ is chosen to be $n=18$ and we then only include states (m,n) with $m \leq 18$ and $n \leq 18-m+1$. We return to consider other schemes of selecting exciton states and examine convergence in Sec. V.

The largest angular momentum included in our simulations is $m=18$ [see Fig. 1(b)]. Thus there are 171 exciton states, and 1140 intraband coherence functions (including populations). Considering all the XCs required, these calculations are fairly intensive.[38] We will show in Sec. V how to make the EXEs more efficient by using a variety of approximations.

IV. EXCITON DYNAMICS: MODERATE INTENSITY EXCITATION

In this section, we consider the nonlinear absorption and population dynamics for a moderate-intensity optical pulse. We choose the pulse intensity such that, in the absence of PSF and exchange, the total exciton density would be $n_{\text{lin}} = 3.0 \times 10^{10}$ cm^{-2}. Due to the suppression caused by PSF and exchange, the total population density obtained in the presence of PSF (n_{non}) and exchange is considerably smaller than n_{lin}. Figure 2 shows the time evolution of the total exciton density and the density of $1s$ excitons when PSF and exchange are included. We see the highest exciton density in the system is $n = 2.6 \times 10^{10}$ cm^{-2}, which is reduced by roughly a factor of 13% from n_{lin}. Moreover, we see that PSF and exchange has resulted in a substantial fraction ($\sim$11%) of the excitons being created in the higher in-plane excited states (HIESs) (the exciton states other than the $1s$ state) rather than in the resonant $1s$ state. We also note that the total exciton density is constant once the pulse has passed (as is expected[13]); however, the $1s$-exciton density oscillates slightly with time due to PSF-induced coupling between different states as described by the term containing $Z^{\mu,\nu}_{\mu_1,\mu_2,\mu_3,\mu_4}$ in Eq. (5).

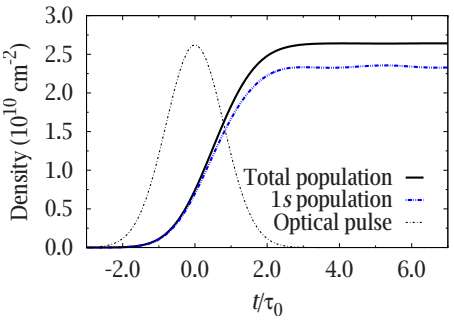

FIG. 2. (Color online) Total exciton density and density in the $1s$ exciton state obtained using the full simulation. $T_{\text{inter}} = T_{\text{decay}} = T_{\text{intra}} = \infty$ is used in obtaining the populations. Also shown is the optical pulse intensity (in arbitrary units).

Before turning to the results for the nonlinear absorption, we consider the population dynamics in more detail. In Fig. 3 we plot the densities of the s states ($m=0$ states) for $n=2$ to $n=18$. The density of $1s$ excitons is not shown because it is too large relative to the others (see Fig. 2). We note that, without PSF and exchange, essentially no exciton population is created in the s states (excluding $1s$ state). Figure 4 shows exciton density distribution of all the $m \neq 0$ HIESs as a function of state energy and time. As discussed above, although the total population is a constant after the optical pulse has passed, the population in individual states continues to oscillate strongly due to the coupling between exciton states. The scattering of excitons out of the $1s$ state into the $m \neq 0$ HIESs is similar to the scattering from a $2s$ state into a $2p$ state seen by Kira and Koch[20] for a quantum wire. It is also related to the scattering out of the $\boldsymbol{K}=0$, $1s$ exciton state into the $K \neq 0$ exciton states seen by Yang *et al.*;[22] although the direct comparison is difficult, given that the systems and laser pulses used are rather different, the fraction of excitons coherently scattered out of the ground exciton state is similar to what we obtain for a similar density.

We see from both Figs. 3 and 4 that the population distribution decays quite rapidly with increasing energy. The reason for this behavior is explained in Appendix B. Its implication on choosing exciton states, and the possibilities of exploiting it in approximations in our simulation are discussed in Sec. V.

Having examined the population dynamics, we now examine the nonlinear optical absorption of the QW. The non-

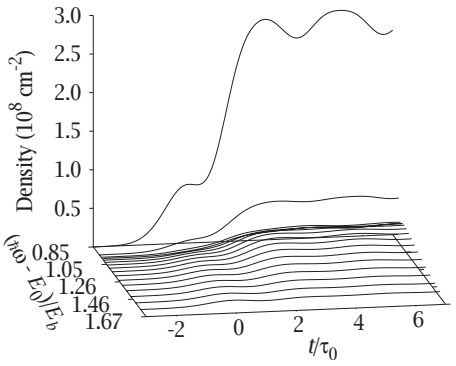

FIG. 3. Population distribution in s exciton states (excluding the $1s$ state). $T_{\text{inter}} = T_{\text{decay}} = T_{\text{intra}} = \infty$ is used.

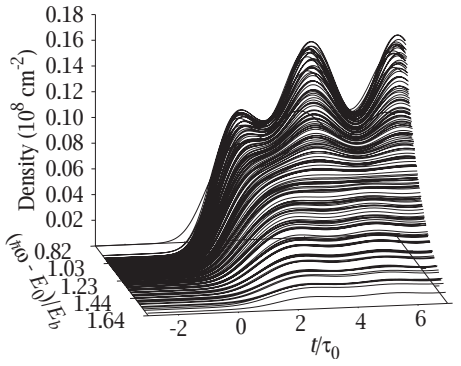

FIG. 4. Population distribution in HIESs with $m \neq 0$. $T_{\text{inter}} = T_{\text{decay}} = T_{\text{intra}} = \infty$ is used.

linear absorption is calculated from the interband polarization as discussed in Sec. II. In Fig. 5, we plot the absorption spectrum for the same pulse used to produce Figs. 2–4. In the same figure, we also plot the absorption spectra obtained in the linear regime (where PSF and exchange effects are neglected) along with the results of some approximate calculations that we describe in Sec. V. The linear result shows an absorption peak at the energy, E_0, of the $1s$ exciton. For the higher-intensity pulse, the absorption spectrum clearly shows a blueshift of approximately 0.21 meV and a reduction in magnitude by approximately 5% from the linear result. These results are consistent with experiments and can be explained using analytical expressions obtained from the EXEs. We discuss this in more detail in Sec. VI. As we shall see below, the effects of HIESs on the nonlinear absorption are very small at this intensity; we discuss their effect at higher intensities in Sec. VII. We close this section by noting that, due to the effects of dephasing and population decay, the total exciton density is reduced from $n=2.6 \times 10^{10}$ cm^{-2} to $n_p = 1.3 \times 10^{10}$ cm^{-2} (the peak value of the exciton density).

V. APPROXIMATION SCHEMES

The results presented in the previous section require rather intensive computations.[38] Thus it is useful to examine possible approximations to reduce the computation time. In this section we examine a number of possible approximations. We first give a brief summary of these approximations in Sec. V A and then present results obtained using some of these approximations in Sec. V B, and discuss the conditions under which the various approximations provide accurate results.

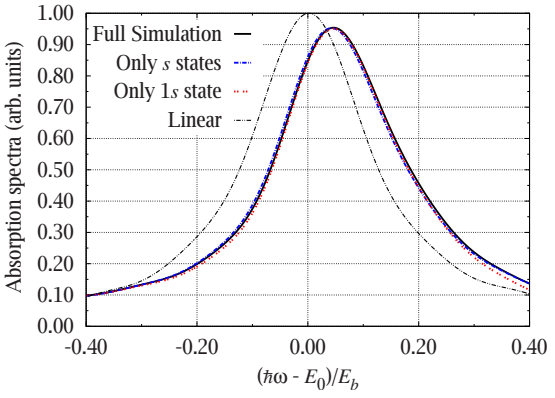

FIG. 5. (Color online) Linear and nonlinear absorption spectra. The thin black line shows the linear absorption spectra while the solid black line shows the nonlinear absorption spectra obtained using the full basis. The blue dashed line and the red dotted line show the nonlinear absorption spectra calculated using the s-state basis and $1s$-state basis, respectively (as discussed in Sec. V B).

A. Possible approximations

If a large number of exciton states are used, the computation is slow primarily due to the large number of *intraband* coherence functions. Thus, there are two ways to reduce the computation time. First, we can reduce the number of intraband coherence functions that are included in the calculation and second, reduce the number of excitonic states included.

To reduce the number of coherence functions, one good approximation is to neglect intraband coherence terms (but not populations) for HIESs with $m > M_{\text{cut}}$ where $M_{\text{cut}} > 0$ is a chosen angular momentum that is much smaller than M_{max}. We find that this approximation is well justified, and have numerically verified that the results obtained with this approximation are in excellent agreement with these obtained using the full EXEs.[23] For the excitation condition considered in the previous section, the difference between the total population, the population distribution, and the absorption spectra are undetectable in Figs. 2 and 5 for $M_{\text{cut}}=4$, which reduces the number of equations from 1158 to 703. This is a significant reduction considering the reduced number of XCs needed.

A second way to reduce the number of equations is to include the populations for HIESs with large m in an approximate way. In Appendix B we show that the populations decay off with energy in a predictable way that can be accurately modeled using a semianalytic expression for $U^{\mu,\nu}_{\mu_1,\mu_2,\mu_3}$. Using this, it may be possible to include the populations for the HIESs approximately by lumping them together into one effective state. We provide a brief discussion of this approximation in the conclusion and explain the behavior in more detail in Appendix B. However, we do not explicitly pursue this approach further in this work.

There are a number of approximations that involve reducing the number of exciton states employed: (1) we can include only the s-exciton states (see Sec. V B), or (2) we can move to the extreme case where the only state employed in the calculation is the $1s$ excitonic state (see Sec. V B).

B. Employing only s-exciton states

In the above discussion, we made approximations with HIESs with $m \neq 0$: we either removed some of them directly or neglected the intraband coherence associated with some of them. These approximations produce quite accurate results, which raises the question: do we really need the HIESs with $m \neq 0$ in our computation at all? To address this question, we now perform simulations with only the s states ($m=0$ states). Doing this reduces the computational time considerably because only 18 exciton states and 171 intraband coherence functions are needed; thus not only does the simulation run

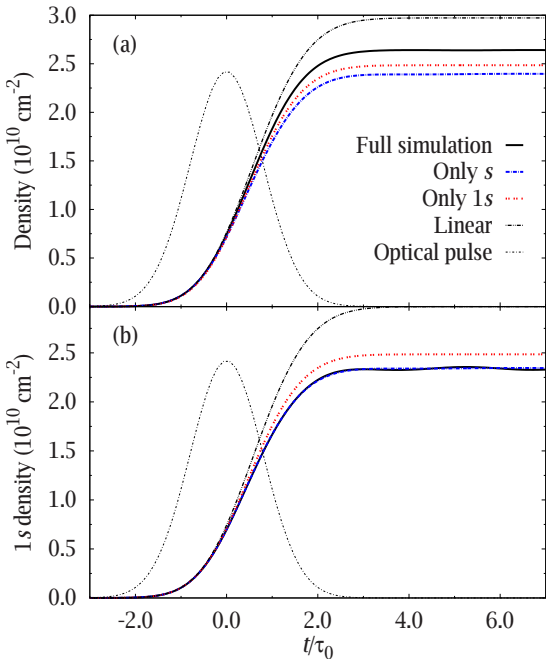

FIG. 6. (Color online) (a) Total exciton density and (b) 1*s* exciton density obtained using different approximation schemes. "Full simulation" indicates the results are obtained using the full simulation (see Sec. IV); "Only *s*" indicates the results are obtained using only *s* exciton states; "Only 1*s*" indicates the results obtained using only the 1*s* exciton state; "Linear" indicates the results are obtained without PSF or exchange.

much faster but far fewer XCs need to be calculated. We call this simulation the *s*-state simulation. As an extreme example, we also perform a simulation employing only the 1*s* state (1*s*-state simulation); in this case, only two EXEs are needed.

In Fig. 5 we plot the nonlinear absorption spectra found from the *s*-state simulation, the 1*s*-state simulation, and the full-basis simulation. As can be seen the differences between the three spectra are only barely discernible. In particular, the difference between the full-basis and *s*-state spectra is roughly the thickness of the line over the full plot range. The results using only the 1*s* state are almost as good, with the main deviation occurring at higher energies, where the contribution of the 2*s* state is becoming important.

To examine these two approximation schemes further, in Fig. 6 we plot the exciton density obtained using the *s*-state and 1*s*-state bases. For comparison, we also show the full-basis results, and the results obtained when PSF and exchange effects are neglected (linear result). Despite the fact that the nonlinear absorption spectra are similar, we find that the *s*-state and 1*s*-state simulations overestimate the total population reduction from the linear result by about 67% and 42%, respectively. However, as seen in Fig. 6(b), the *s*-state simulation yields a reasonably accurate value for the density of 1*s* excitons while the 1*s*-state simulation underestimates the reduction in 1*s*-exciton density by about 22%.

Although the *s*-state simulation provides an accurate value for the density of 1*s* excitons, it does not do as well for the higher *s*-exciton populations. In Fig. 7, we plot densities

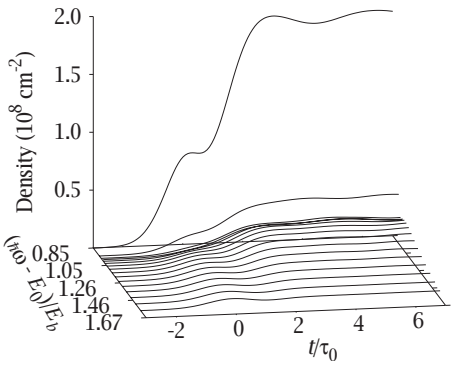

FIG. 7. Population density distribution of *s*-exciton states for the simulation using only *s* excitons states.

of the various *ns* excitons ($n>1$). Comparing to Fig. 3, we see in particular that the density of 2*s* excitons is underestimated by roughly 30%.

We conclude from the above results that, for the resonant excitation that we have used, acceptable accuracy can be obtained for the nonlinear absorption spectra using simulations where only the *s* states or even only the 1*s* state are included. These approximations work well for several reasons: first, because only the 1*s* exciton is directly excited (in the linear regime), we expect it to be dominant in the system; second because only the *s* excitons are optically active, only they can contribute directly to the nonlinear absorption; third, for the intensity considered here, the coupling of the 1*s* exciton to the $m\neq 0$ excitons is relatively small and so their influence on the absorption is almost negligible. We note that, however, if the excitation pulse intensity is increased, it is necessary to include the $m\neq 0$ HIESs; we find that with this pulse, the HIESs start to affect the nonlinear absorption significantly when the total carrier density is about 5.0×10^{10} cm^{-2} (see Sec. VII). We also note that if the optical pulse has a higher central frequency (or spectral width), such that it excites the higher *s*-exciton states directly, then it is important to include the additional resonant *s* states in the simulation.

VI. BLUESHIFT AND BLEACHING OF THE EXCITON RESONANCE

It is well known that in a QW, PSF results in the blueshift and bleaching of the exciton resonance that have been observed.[1–3,8] We see from the results of the previous sections that at moderate densities, the nonlinear absorption can be accurately calculated using a basis of only the 1*s* excitons. In this section, we use this result to obtain approximate expressions for the blueshift and bleaching of the 1*s* exciton peak as a function of density. The analytical expressions offer a simple way to understand and calculate the nonlinearities in an optically excited QW.

From Eq. (4), we have

$$i\hbar\frac{d}{dt}\langle B_0^\dagger\rangle + \left(E_0 - 2\sum_{\mu_2,\mu_3} R^0_{0,\mu_2,\mu_3}\langle B^\dagger_{\mu_2}B_{\mu_3}\rangle\right)\langle B_0^\dagger\rangle$$
$$= -i\hbar\frac{\langle B_\mu^\dagger\rangle}{T_{\text{inter}}^{\text{EXE}}} + 2\sum_{\mu_1\neq 0,\mu_2,\mu_3} R^0_{\mu_1,\mu_2,\mu_3}\langle B^\dagger_{\mu_1}\rangle\langle B^\dagger_{\mu_2}B_{\mu_3}\rangle$$
$$+ \mathcal{E}(t)\cdot \boldsymbol{M}^*_{cv}\left(C_\mu - 2\sum_{\mu_1,\mu_2} C_{\mu,\mu_1,\mu_2}\langle B^\dagger_{\mu_1}B_{\mu_2}\rangle\right), \quad (10)$$

where we have singled out $1s$ excitons for investigation. If the $1s$ ($\mu=0$ state) excitons dominate (which is the case of resonant excitation of the $1s$ exciton state), we can neglect all states except the $1s$ excitons in the above equation and keep only $\mu_i=(1,0)$ in the sums in the above equation. From this, we see that the energy shift in the $1s$ exciton resonance is given approximately by

$$\frac{\Delta E_{1s}}{E_{1s}} = -\frac{2R^0_{0,0,0}}{E_{1s}}\langle B_0^\dagger B_0\rangle. \quad (11)$$

Similarly, the reduction (bleaching) in the oscillator strength, which is given by the last term in Eq. (10), is simply

$$\frac{\Delta f_{1s}}{f_{1s}} = \frac{C_0^2 - (C_0 - 2C_{0,0,0}\langle B_0^\dagger B_0\rangle)^2}{C_0^2} \quad (12)$$

$$\simeq 4\frac{C_{0,0,0}}{C_0}\langle B_0^\dagger B_0\rangle. \quad (13)$$

From Eqs. (11) and (13), we find that $\Delta E_{1s}/E_{1s}$ and $\Delta f_{1s}/f_{1s}$ are linearly related,

$$\frac{\Delta E}{E_{1s}} = \gamma\frac{\Delta f_{1s}}{f_{1s}}, \quad (14)$$

where

$$\gamma = -\frac{C_0 R^0_{0,0,0}}{2C_{0,0,0}E_{1s}}. \quad (15)$$

This linear relation is very useful in comparing to experimental results[3,8] because it does not require the accurate measurement of exciton population densities.

We consider first the blueshift and the bleaching of excitons in a strict 2D system. We know the expression for the $1s$ exciton wave function is[15,23]

$$\psi_{1s}(\boldsymbol{r}) = \sqrt{\frac{2}{\pi}}\frac{2}{a_0}\exp\left(-\frac{2r}{a_0}\right), \quad (16)$$

where a_0 is the Bohr radius of a $1s$ exciton in bulk semiconductors. Its Fourier transform is given by[2,23]

$$c^{\boldsymbol{p}}_{1s} = c^p_{1s} = \sqrt{\frac{2\pi}{S}}\frac{a_0}{\left[1+\left(\frac{a_0 p}{2}\right)^2\right]^{3/2}}, \quad (17)$$

where S is the area in the plane. Using this result, it can be shown that

$$R^0_{0,0,0} = -\left(\frac{16\pi a_{2D}^2}{S}\right)\left(1 - \frac{315\pi^2}{2^{12}}\right)E_{1s}, \quad (18)$$

$$C_0 = \sqrt{\frac{S}{2\pi}}\frac{4}{a_0}, \quad (19)$$

and

$$C_{0,0,0} = \sqrt{\frac{2\pi}{S}}\frac{4a_0}{7}, \quad (20)$$

where $a_{2D}=a_0/4$ is the radius of a 2D $1s$ exciton.[2] We note that the two terms (1 and $315\pi^2/2^{12}$) in Eq. (18) are due to PSF and exchange, respectively. The net effect causes the blueshift observed in the absorption spectra.

From Eq. (18), the magnitude of the $1s$ exciton energy shift is given by

$$\Delta E_{1s} = 32\pi n_{1s}a_{2D}^2\left(1 - \frac{315\pi^2}{2^{12}}\right)E_{1s}, \quad (21)$$

where $n_{1s}\equiv\langle B_0^\dagger B_0\rangle/S$ is the density of $1s$ excitons. This result is just the expression below Eq. (12) in Ref. 2 (see Ref. 39). Using Eqs. (19) and (20), the fractional change in oscillator strength $\Delta f/f_{1s}$ is

$$\frac{\Delta f}{f_{1s}} \simeq \frac{128\pi}{7}a_{2D}^2 N_{1s}, \quad (22)$$

which agrees with Eq. (9) of Ref. 2 (see Ref. 40). Therefore, for an ideal 2D system, we have

$$\gamma = \frac{7}{4}\left(1 - \frac{315\pi^2}{2^{12}}\right) \approx 0.422. \quad (23)$$

For the QW we have investigated in Sec. IV, the numerical values for the XCs are

$$C_0 = 7.52\times 10^1, \quad (24)$$

$$C_{0,0,0} = 2.54\times 10^{-2}, \quad (25)$$

$$R^0_{0,0,0} = -5.54\times 10^{-4}. \quad (26)$$

We note that because $R^0_{0,0,0}$ is negative, it causes a blueshift in the $1s$ exciton resonance. Plugging these numbers into Eq. (15), we find

$$\gamma = -\frac{C_0 R^0_{0,0,0}}{5C_{0,0,0}} = 0.33. \quad (27)$$

This value of γ falls in the range of 0.3–1.0 that have been experimentally observed and theoretically predicted.[1,8,41] The linear relation in Eq. (14) has been verified in our numerical simulations; the value of γ obtained is $\sim$0.24, which is smaller than the value of 0.33 given largely because, in our simulations, the exciton populations are gradually built up in the QW and we cannot assume a simple static population.

Before closing this section, we give a brief summary of the experimental work on the excitonic resonance. Most experimental studies on the blueshift of the exciton resonance employ a pump-probe setup using ultrashort laser pulses.[1,3,8] Excitons can be created using either resonant or nonresonant excitation schemes.[1] For the nonresonant (band to band) excitation, where hot carriers are created first, the exciton absorption structure disappears immediately after (within

~1 ps) the excitation. This excitonic bleaching is due to free-carrier screening of the Coulomb interaction. In this period of time, no blueshift is observed. After a period of ~10 ps, the excitonic absorption structure reappears with a blueshift of the peak of the 1*s* exciton. For the resonant excitation, an instantaneous blueshift is observed without large excitonic bleaching, and it takes about 400 ps for the exciton resonance to gradually resume its normal position.[1] This time scale is approximately determined by the exciton lifetime. The well-size dependency of the blueshift has been also investigated,[3] where samples of different well and barrier sizes were tested. For well sizes wider than 100 Å, the blueshift is negligibly small.

With the advance of spectroscopy techniques, the differential absorption/transmission spectroscopy[42] was applied to the study of exciton dynamics in quantum wells.[6,8] In particular, the authors using this technique try to distinguish two nonlinear effects, the interaction between excitons and free-carrier screening, by fitting absorption/transmission spectra. It is concluded that the bleaching due to PSF and the exchange interaction is approximately two times larger than that due to free-carrier screening with a carrier density of $\sim 2.0 \times 10^{11}$ cm^{-2}.[8,32]

In experiments, the relation between peak shift and bleaching has been measured.[3,8] A very good linear relation was verified although the constant value γ varies over a wide range. It is shown to be ~1 for narrow quantum wells (40 Å GaAs well, 100 Å $Ga_{0.7}Al_{0.3}As$ barrier; see Ref. 3), and ~0.8 for slightly wider wells (75 Å GaAs well, 100 Å $Ga_{0.66}Al_{0.34}As$ barrier; see Ref. 8), but a value of 0.3 has also been reported (75 Å GaAs well, GaAlAs barrier, width not reported; see Ref. 41). Several factors are responsible for the wide distribution of observed γ values: the influence of well width and lattice temperature,[41] the influence of free carriers,[8] and the dipole interaction between excitons in different wells (most experiments use multiple quantum wells).[43] An accurate determination of the constant value γ needs to consider these factors and is highly nontrivial.

VII. EXCITON DYNAMICS: HIGH DENSITY ABSORPTION SPECTRA AND THE ROLE OF HIESS

For the resonant excitation at the moderate density of $n = 1.3 \times 10^{10}$ cm^{-2} considered in the previous sections, we found that the coupling of *s* states and the HIESs played only a small role in determining the nonlinear optical absorption. However, if the pulse intensity is increased, the situation changes. To understand the effect of the HIESs, we now consider the absorption spectra at the considerably higher density of $n = 5.0 \times 10^{10}$ cm^{-2}. We decrease the pulse duration to $\tau_p = 107.6$ fs, so as to directly excite carriers in the bound as well as continuum sates. In this way, we can clearly see the effects of the exciton states both above and below the band edge on the absorption spectra. All other parameters (ω_c, T_{inter}, T_{intra}, and T_{decay}) are the same as used in Sec. IV.

In Fig. 8, we plot the absorption spectra of the QW obtained using three different subsets of the exciton states at the peak density of $n = 5.0 \times 10^{10}$ cm^{-2}. The three different simulations include (1) the full set of 171 states shown in Fig. 1(b), (2) only the *s* states, and (3) only the 1*s* state. For comparison, we also show the linear absorption spectra (where PSF and exchange effects are neglected). The linear result has a 1*s* absorption peak at E_0, and an absorption step at around $0.8E_b$ that corresponds to the onset of 2*s* and band-edge absorption. For the high-density excitation, the 1*s* exciton resonance shows a blueshift and bleaching due to the combined PSF and exchange effects.

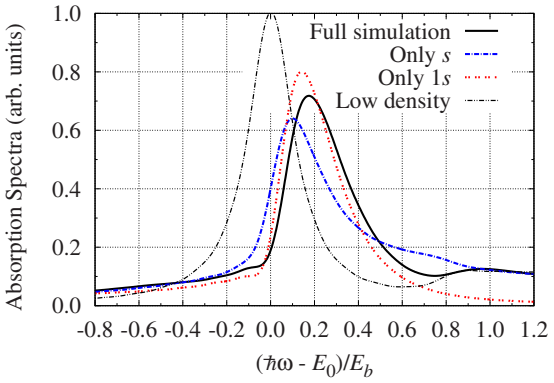

FIG. 8. (Color online) Absorption spectra for the high-density excitation condition obtained with different sets of exciton states: full-basis simulation (solid black line), the *s*-state simulation (blue dashed line), and the 1*s*-state simulation (red dotted line). Also shown is the linear result (thin black line) obtained by neglecting PSF and exchange. The legends have the same meaning as in Fig. 6.

As we can see from Fig. 8, the HIESs indeed make a considerable difference in the absorption spectrum. For example, for the 1*s* absorption peak: the *s*-state simulation underestimates the blueshift considerably but overestimates the peak saturation while the 1*s*-state simulation slightly underestimates the blueshift and also underestimates the bleaching. In Fig. 9 we plot the population density evolution for 1*s* excitons using the three different simulations to help understand the absorption spectra. We find that the simulation using only 1*s* exciton has a considerably larger 1*s* population than found in the other two simulations. This larger population is expected in the 1*s*-state simulation because there are fewer states to reduce the effective oscillator strength of the 1*s* exciton (as discussed in Sec. VI). Thus, we observed a larger 1*s* oscillator strength. The larger 1*s* population also

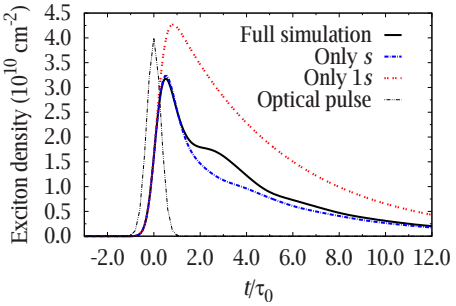

FIG. 9. (Color online) Population density of the 1*s* exciton obtained using different subsets of exciton states for the high-density excitation condition of Sec. VII. In this simulation we use $T_{\text{intra}} = \infty$ as was used in the nonlinear absorption calculation. The legends have the same meaning as in Fig. 6.

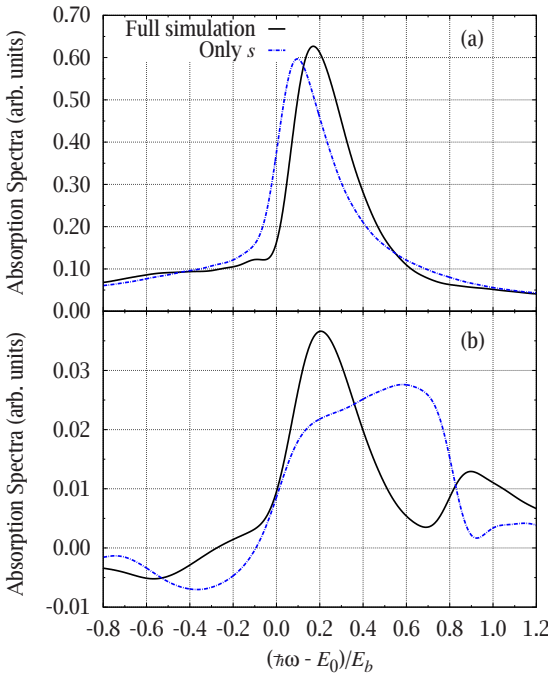

FIG. 10. (Color online) The absorption spectra for the high-density excitation condition calculated from the polarization due only to (a) only the 1*s* state and (b) the 2*s* state. The solid black line is obtained using the full-basis simulation while the blue dashed line is obtained using the *s*-state basis simulation. The legends have the same meaning as in Fig. 6.

accounts for the fact that the 1*s*-state simulation has a larger blueshift than that obtained in the simulation using all the *s* exciton states.

We also see from Fig. 9 that in the full simulation, the 1*s* exciton population has a longer lifetime than in the *s*-state simulation. This longer lifetime arises from coupling of the $m \neq 0$ HIESs populations and intraband coherence back to the 1*s*-state population (and interband coherence function), which can be approximately understood as scattering of the $m \neq 0$ HIESs excitons back into the 1*s* state [see Eqs. (4) and (5)]. This fact explains why the full simulation has a larger 1*s* peak shift than the *s*-state simulation even though they have almost identical similar peak values for the 1*s* exciton population.

The other feature of Fig. 8 that stands out is the large difference near the band edge between the full simulation and the *s*-state simulation. Although it is obvious that including only the 1*s*-exciton state will not capture the band edge, it is somewhat surprising that the *s*-state simulation gives such a different result from the full simulation. The origin of this difference can be partially understood by examining the contributions of the different excitonic states to the absorption spectrum. In Fig. 10(a) we plot the nonlinear absorption due to only the 1*s* state while in Fig. 10(b), we plot the absorption due to just the 2*s* state obtained using the full simulation and the simulation using only *s* states. The result for the 1*s* state shows that, in agreement with Fig. 8 the full simulation gives a somewhat larger blueshift in the 1*s* peak. However, the difference in the bleaching is not nearly as great as expected. This can be understood by looking at the contribution from the 2*s* state in Fig. 10(b) where there is a large peak for both simulations near $0.2E_b$. This arises because some of the character of the 1*s* state is mixed into the 2*s* state via the intraband coherence. Because this peak is larger in the full simulation, we expect a larger overall absorption peak for the full simulation, as observed. The more striking difference between the two results for the 2*s* absorption is that there is a much greater redshift in the 2*s* peak (near $0.8E_b$) in the *s*-state simulation than in the full simulation. It is this difference that gives the different response in the absorption spectrum near the band edge. It is well known that the band-edge states exhibit a redshift as the population density is increased.[44] However, we see that the $m \neq 0$ HIESs strongly influence the magnitude of this shift. In fact, this influence appears to be greater than that of the $m=0$ HIESs. This could perhaps be tested experimentally by using a terahertz field to populate the $m=1$ exciton states.

VIII. CONCLUSION

Using an excitonic formalism, we have investigated the dynamics and nonlinear optical response of excitons photoexcited by a short optical pulse in a QW. We have shown that our excitonic approach provides an accurate and efficient way of calculating the optical response of a QW, especially for resonant excitation of the 1*s* exciton with moderate-intensity pulses. We have also investigated the excitonic dynamics in a QW using an analytical approach, and derived the relationship between the blueshift and the bleaching of the 1*s* exciton resonance. Using a combination of numerical and analytic results, we have demonstrated that the EXEs are a powerful tool for calculating and understanding some important features of the carrier dynamics involved in nonlinear interband dynamics in a QW.

We have shown that, at moderate densities, if the optical pulse is resonant on the 1*s* exciton then the excitonic approach yields accurate results even if the 1*s* exciton is the only state included in our calculations. This shows that, in this limit, this approach would be much more efficient than using an electron-hole basis such as employed in the SBEs. We have also shown that, at higher density, the nonlinear absorption is strongly affected by the coupling of the 1*s* states to both optically active and inactive higher in-plane excited exciton states.

We have examined a variety of possible approximations to increase the efficiency of the computation. These approximations focus on reducing the number of equations that are related to the HIESs with $m \neq 0$. Based on our analysis of the $m \neq 0$ HIESs in Appendix B, we propose a possible further approximation that keeps only some "representative" population terms for the $m \neq 0$ HIESs. With this approximation, one could perhaps substantially reduce the number of dynamical equations. We leave the investigation of this approximation to future work.

The exciton approach can also be used to investigate the nonlinear intraband dynamics involved when both an optical and terahertz field are present. With the advance of ultrafast THz spectroscopy, it has been argued that to obtain detailed information such as exciton populations, conventional ex-

perimental techniques should be supplemented by direct intraexcitonic spectroscopy using the available terahertz light sources. For example, it offers a systematic approach to investigate the effects of PSF and exchange on the intraband transitions between $1s$ and $2p$ exciton states.[33] It also offers the possibility of examining the effect of the $m \neq 0$ states on the shift in the $1s$ and band-edge absorption energies.[10–12,45] Our excitonic approach will serve as a useful theoretical tool to understand these exciting experiments and we will apply it to this class of problems in future work.

ACKNOWLEDGMENTS

This work was supported in part by the Natural Sciences and Engineering Research Council of Canada. We acknowledge the use of the HPCVL computing facility at Queen's University. D.W. also acknowledges the partial support from the Ministry of Science and Technology of China (973 Program No. 2006CB921602).

APPENDIX A: OBTAINING EXCITONIC COEFFICIENTS

The application of the excitonic formalism to a specific system can be divided into two stages. The first stage is to obtain the XCs from the exciton wave functions; the second stage is to use the EXEs to compute excitonic dynamics for the given system. In this section, we focus on the first stage and show how the XCs can be obtained for a QW.

The XCs in the first dynamic equation [Eq. (4)] are given by

$$R^{\mu}_{\mu_1,\mu_2,\mu_3} = R1^{\mu}_{\mu_1,\mu_2,\mu_3} - R2^{\mu}_{\mu_1,\mu_2,\mu_3}, \tag{A1}$$

$$R1^{\mu}_{\mu_1,\mu_2,\mu_3} = \sum_{\boldsymbol{k},\boldsymbol{p}} V_{\boldsymbol{p}-\boldsymbol{k}} c^{\boldsymbol{p}}_{\mu} c^{\boldsymbol{p}*}_{\mu_1} c^{\boldsymbol{k}*}_{\mu_2} c^{\boldsymbol{k}}_{\mu_3}, \tag{A2}$$

$$R2^{\mu}_{\mu_1,\mu_2,\mu_3} = \sum_{\boldsymbol{k},\boldsymbol{p}} V_{\boldsymbol{p}-\boldsymbol{k}} c^{\boldsymbol{p}}_{\mu} c^{\boldsymbol{p}*}_{\mu_2} c^{\boldsymbol{k}*}_{\mu_1} c^{\boldsymbol{p}}_{\mu_3}, \tag{A3}$$

$$C_{\mu} = \sum_{\boldsymbol{p}} c^{\boldsymbol{p}}_{\mu}, \tag{A4}$$

$$C_{\mu,\mu_1,\mu_2} = \sum_{\boldsymbol{p}} c^{\boldsymbol{p}}_{\mu} c^{\boldsymbol{p}*}_{\mu_1} c^{\boldsymbol{p}}_{\mu_2}, \tag{A5}$$

where $V_{\boldsymbol{p}}$ is the Fourier transformation of the effective Coulomb interaction in the QW.[23] $R1^{\mu}_{\mu_1,\mu_2,\mu_3}$ is due to the exchange interaction while $R2^{\mu}_{\mu_1,\mu_2,\mu_3}$ and C_{μ,μ_1,μ_2} are from PSF.

The second dynamic equation [Eq. (5)] contains

$$Z^{\mu,\nu}_{\mu_1,\mu_2,\mu_3,\mu_4} = S^{\mu,\nu}_{\mu_1,\mu_2,\mu_3,\mu_4} - T^{\mu,\nu}_{\mu_1,\mu_2,\mu_3,\mu_4}, \tag{A6}$$

$$S^{\mu,\nu}_{\mu_1,\mu_2,\mu_3,\mu_4} = \sum_{\boldsymbol{k},\boldsymbol{p},\boldsymbol{q}} (V_{\boldsymbol{p}-\boldsymbol{k}} - V_{\boldsymbol{q}-\boldsymbol{k}})(1-\delta_{\boldsymbol{p},\boldsymbol{k}})(1-\delta_{\boldsymbol{k},\boldsymbol{q}}) \times c^{\boldsymbol{p}}_{\mu} c^{\boldsymbol{q}*}_{\nu} c^{\boldsymbol{p}*}_{\mu_1} c^{\boldsymbol{k}*}_{\mu_2} c^{\boldsymbol{k}}_{\mu_3} c^{\boldsymbol{q}}_{\mu_4}, \tag{A7}$$

$$T^{\mu,\nu}_{\mu_1,\mu_2,\mu_3,\mu_4} = \sum_{\boldsymbol{k},\boldsymbol{p},\boldsymbol{q}} (c^{\boldsymbol{p}}_{\mu} c^{\boldsymbol{q}*}_{\nu} V_{\boldsymbol{k}-\boldsymbol{p}} - c^{\boldsymbol{k}}_{\mu} c^{\boldsymbol{p}*}_{\nu} V_{\boldsymbol{q}-\boldsymbol{p}}) \times (1-\delta_{\boldsymbol{p},\boldsymbol{k}})(1-\delta_{\boldsymbol{p},\boldsymbol{q}}) c^{\boldsymbol{k}*}_{\mu_1} c^{\boldsymbol{p}*}_{\mu_2} c^{\boldsymbol{p}}_{\mu_3} c^{\boldsymbol{q}}_{\mu_4}, \tag{A8}$$

$$U^{\mu,\nu}_{\mu_1,\mu_2,\mu_3} = \sum_{\boldsymbol{p},\boldsymbol{q}} c^{\boldsymbol{p}}_{\mu} c^{\boldsymbol{q}*}_{\nu} c^{\boldsymbol{p}*}_{\mu_1} c^{\boldsymbol{p}}_{\mu_2} c^{\boldsymbol{q}}_{\mu_3} (1-\delta_{\boldsymbol{p},\boldsymbol{q}}), \tag{A9}$$

where $S^{\mu,\nu}_{\mu_1,\mu_2,\mu_3,\mu_4}$ is due to the exchange interaction, and $T^{\mu,\nu}_{\mu_1,\mu_2,\mu_3,\mu_4}$ and $U^{\mu,\nu}_{\mu_1,\mu_2,\mu_3}$ are due to PSF.

As we can see, the building blocks for the XCs are $c^{\boldsymbol{q}}_{\mu}$. These can be obtained from the excitonic envelope wave functions simply by inverting Eq. (2) to obtain

$$c^{\boldsymbol{p}}_{\mu} = \int d^2\boldsymbol{r} dz_e dz_h f^*_e(z_e) f^*_h(z_h) \times \frac{\exp(-i\boldsymbol{p}\cdot\boldsymbol{r})}{\sqrt{A}} \Phi_{\mu}(\boldsymbol{r}, z_e, z_h). \tag{A10}$$

Thus, all the required coefficients can be obtained in principle if we have the exciton envelope functions and energies. We now turn to the calculation of the exciton envelope functions.

The label, μ for the excitonic state $\Phi_{\mu}(\boldsymbol{r}, z_e, z_h)$, can be written as the pair $\mu=(n,m)$, where $m\hbar$ is the z component of orbital angular momentum of the exciton and n is the principle quantum number. To determine the QW excitonic states (bound and unbound) numerically, we use the same approach that we have used in the past to determine the so-called two-well states in a superlattice.[25,46] The exciton wave function $\Phi_{n,m}(\boldsymbol{r}, z_e, z_h)$ in a quantum well is one special case of the two-well states where the electron and hole reside in the same well. To obtain these, we expand them in terms of the energy eigenstates for noninteracting electron-hole pairs in a cylindrical geometry. That is, we write[25,46]

$$\Phi_{n,m}(\boldsymbol{r}, z_e, z_h) = f_e(z_e) f(z_h) \sum_{k_i} A^{n,m}_{k_i} g^m_{k_{i,m}}(r,\phi),$$

where $\boldsymbol{r}=(r,\phi)$ and $g^m_{k_{i,m}}(r,\phi)$ is a the noninteracting pair eigenstate in the plane, and is given by

$$g^m_{k_{i,m}}(r,\phi) \equiv \frac{\exp(im\varphi)}{R\sqrt{\pi}|J'_m(k_i R)|} J_m(k_{i,m} r), \tag{A11}$$

where $J_m(x)$ is the mth Bessel function. To obtain a discrete basis set, we have chosen the solution space in the plane to be a circle of radius R and applied hard boundary conditions; with this boundary condition, $k_{i,m}$ is given the ith zero of $J_m(kR)$. The normalization has been chosen such that

$$\int_0^{2\pi} d\phi \int_0^R r d\rho g^m_{k_{i,m}}(r,\phi) g^m_{k_{j,m}}(r,\phi) = \delta_{i,j}. \tag{A12}$$

Using the above expansion with a radius, R, of 40 exciton Bohr radii, and using a set of 400 basis functions for each m, we numerically solve for the eigenenergies E_{μ} and the expansion coefficients, $A^{n,m}_{k_i}$.

Using Eq. (A11) and letting $\boldsymbol{p}=p(\cos\theta, \sin\theta)$, $\boldsymbol{r}=r(\cos\phi, \sin\phi)$, we obtain

$$c^{p}_{n,m} = \frac{2\sqrt{\pi}}{L}\exp\left[im\left(\theta - \frac{\pi}{2}\right)\right]J_m(pR) \times \sum_{k_{i,m}} A^{n,m}_{k_{i,m}} \frac{k_{i,m}\,\mathrm{sgn}[J'_m(k_{i,m}R)]}{k^2_{i,m} - p^2}, \quad \text{(A13)}$$

where $\mathrm{sgn}(x)$ returns the sign of x.

The XCs are obtained from the c^{p}_{μ} by using Eqs. (A1)–(A9). The procedure for calculating XCs involves converting the sums in these equations into integrals and carrying out the integrals numerically. This approach is straightforward so we do not present the details here but refer the reader to Ref. 23.

APPENDIX B: UNDERSTANDING POPULATION DYNAMICS IN HIESS

In this appendix, we discuss the populations in the HIESs with $m \neq 0$ and show that they are largely determined by $U^{\mu,\nu}_{\mu_1,\mu_2,\mu_3}$. We then present an approximate expression for the $U^{\mu,\nu}_{\mu_1,\mu_2,\mu_3}$, which explains the main features of these XCs that could be used to simplify the dynamics calculations.

It can be shown that the population of excitons in HIESs with $m \neq 0$ are determined largely by $U^{\mu,\nu}_{\mu_1,\mu_2,\mu_3}$ and $Z^{\mu,\nu}_{\mu_1,\mu_2,\mu_3,\mu_4}$, as these excitons are only created through PSF and the exchange interaction. From Eq. (5), for the populations of $m \neq 0$ HIESs, we have

$$i\hbar\frac{d}{dt}\langle B^{\dagger}_{\mu}B_{\mu}\rangle = 2\sum_{\mu_1,\mu_2,\mu_3,\mu_4} Z^{\mu,\mu}_{\mu_1,\mu_2,\mu_3,\mu_4}\langle B^{\dagger}_{\mu_1}B_{\mu_4}\rangle\langle B^{\dagger}_{\mu_2}B_{\mu_3}\rangle \quad \text{(B1)}$$

$$-2\sum_{\mu_1,\mu_2,\mu_3}[\mathcal{E}(t)\cdot \boldsymbol{M}^{*}_{cv}U^{\mu,\mu}_{\mu_1,\mu_2,\mu_3}\langle B^{\dagger}_{\mu_1}B_{\mu_2}\rangle\langle B_{\mu_3}\rangle - \mathcal{E}(t)\cdot \boldsymbol{M}_{cv}U^{\mu,\mu*}_{\mu_3,\mu_2,\mu_1}\langle B^{\dagger}_{\mu_1}\rangle\langle B^{\dagger}_{\mu_2}B_{\mu_3}\rangle], \quad \text{(B2)}$$

where we have dropped terms related to population decay; terms involving C_{μ} do not appear because $C_{\mu}=0$ if μ labels a state with $m \neq 0$. From the above expression, it is clear that $U^{\mu,\mu}_{\mu_1,\mu_2,\mu_3}$ largely determines the creation of population in each HIESs while $Z^{\mu,\nu}_{\mu_1,\mu_2,\mu_3,\mu_4}$ couples different exciton states, making the population in each HIESs to oscillate. Thus, some insight into $U^{\mu,\nu}_{\mu_1,\mu_2,\mu_3}$ helps explain why the populations of HIESs with $m \neq 0$ decay quickly with increasing energy as shown in Fig. 4.

Figure 11(a) shows numerical values of $U^{\mu,\mu}_{0,0,0}/U^{0,0}_{0,0,0}$ versus the exciton energy. Here and in the following, we use $\mu=0$ to indicate the $1s$ exciton state. As we can see, the magnitude of $U^{\mu,\mu}_{0,0,0}$ decreases quickly with increasing exciton energy.

We now derive a simple expression for $U^{\mu,\mu}_{0,0,0}$ with approximations. If μ is a HIES with $m \neq 0$, we know

$$\frac{U^{\mu,\mu}_{0,0,0}}{U^{0,0}_{0,0,0}} = \frac{-C_{\mu,\mu,0,0,0}}{C_{0,0,0} - C_{0,0,0,0,0}}. \quad \text{(B3)}$$

We thus need to know $C_{\mu,\mu,0,0,0}$, which is given by

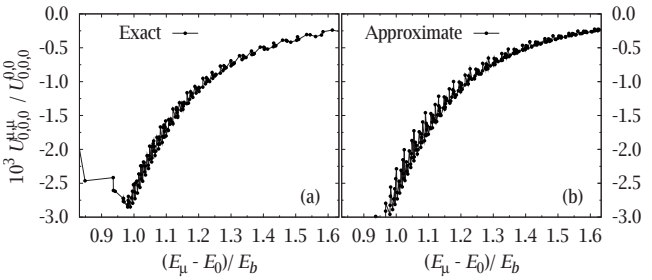

FIG. 11. The ratio $U^{\mu,\mu}_{0,0,0}/U^{0,0}_{0,0,0}$ as a function of energy calculated using (a) the exact numerical expression of Eq. (B3) and (b) the approximate expression of Eq. (B6).

$$C_{\mu,\mu,0,0,0} \approx (c^{k_{n,m}}_{0})^3\frac{L^2}{2\pi}\int dk k c^{k}_{\mu}c^{k*}_{\mu} \quad \text{(B4)}$$

$$= (c^{k_{n,m}}_{0})^3. \quad \text{(B5)}$$

The above approximation uses the fact that, since $\mu=(n,m)$ is a HIES, c^{k}_{μ} only has large values in a small region of k and it peaks at $k_{n,m}$. In contrast, $c^{k}_{(0,0)}$ spreads over a large region of k. As an example, this behavior is shown in Fig. 12 where we plot $(c^{k}_{(0,0)})^3$ and $k(c^{k}_{(10,5)})^2$ as functions of k. This property is exploited in Eq. (B5) to simplify the expression.

Using the above result, we obtain the following approximate expression for $U^{\mu,\mu}_{0,0,0}/U^{0,0}_{0,0,0}$:

$$\frac{U^{\mu,\mu}_{0,0,0}}{U^{0,0}_{0,0,0}} \simeq -\frac{(c^{k_{\mu}}_{(0,0)})^3}{U^{0,0}_{0,0,0}}, \quad \text{(B6)}$$

where $c^{p}_{(0,0)}$ is given by

$$c^{p}_{(0,0)} = \frac{2\sqrt{\pi}}{L}\sum_{k} A^{0}_{k}\frac{kJ_0(pR)}{(k^2-p^2)}\mathrm{sgn}[J_1(kR)]. \quad \text{(B7)}$$

The numerical results obtained with this expression are shown in Fig. 11(b). As we can see, the two results agree well (to within about 15% difference), indicating that the approximation for HIESs is valid. This explains the fast decay of the populations in the $m \neq 0$ HIESs seen in Fig. 4.

Although we use the exact expression for $U^{\mu,\mu}_{\mu_1,\mu_2,\mu_3}$ in all our simulations, the approximate expression obtained here

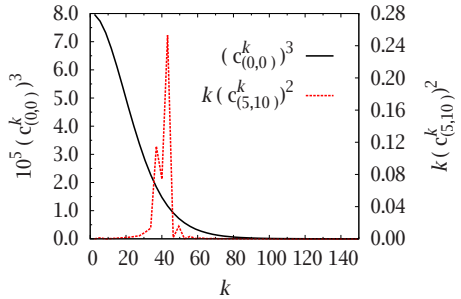

FIG. 12. (Color online) $(c^{k}_{(0,0)})^3$, $k(c^{k}_{(10,5)})^2$ as a function of k. Compared with the smooth function, $(c^{k}_{(0,0)})^3$, $k(c^{k}_{(10,5)})^2$ peaks in a narrow region of k. This property can be used in integrals that involve both functions as in Eq. (B5).

can be used to reduce the XCs calculations. Furthermore, given Eq. (B2), we expect the population N_μ in the exciton state μ to decay off rapidly with increasing E_μ as is found in Fig. 4. As we discuss in Sec. V A and the conclusion, this property could be the basis for an approximation scheme to simplify the treatment of HIESs.

*dignam@physics.queensu.ca

[1] N. Peyghambarian, H. M. Gibbs, J. L. Jewell, A. Antonetti, A. Migus, D. Hulin, and A. Mysyrowicz, Phys. Rev. Lett. **53**, 2433 (1984).

[2] S. Schmitt-Rink, D. S. Chemla, and D. A. B. Miller, Phys. Rev. B **32**, 6601 (1985).

[3] D. Hulin, A. Mysyrowicz, A. Antonetti, A. Migus, W. T. Masselink, H. Morkoç, H. M. Gibbs, and N. Peyghambarian, Phys. Rev. B **33**, 4389 (1986).

[4] U. Neukirch and K. Wundke, Phys. Rev. B **55**, 15408 (1997).

[5] G. Manzke, Q. Y. Peng, K. Henneberger, U. Neukirch, K. Hauke, K. Wundke, J. Gutowski, and D. Hommel, Phys. Rev. Lett. **80**, 4943 (1998).

[6] F. Chen, M. C. Cheung, P. M. Sweeney, W. D. Kirkey, M. Furis, and A. N. Cartwright, J. Appl. Phys. **93**, 4933 (2003).

[7] M. T. Portella-Oberli, V. Ciulin, M. Kutrowski, T. Wojtowicz, and B. Deveaud, Phys. Status Solidi B **238**, 513 (2003).

[8] M. Choi, K.-C. Je, S.-Y. Yim, and S.-H. Park, Phys. Rev. B **70**, 085309 (2004).

[9] M. Seemann, F. Kieseling, H. Stolz, M. Florian, G. Manzke, K. Henneberger, and D. Hommel, Phys. Status Solidi B **245**, 1093 (2008).

[10] J. Wang, I. Cotoros, K. M. Dani, X. Liu, J. K. Furdyna, and D. S. Chemla, Phys. Rev. Lett. **98**, 217401 (2007).

[11] K. M. Dani, I. A. Cotoros, J. Wang, J. Tignon, D. S. Chemla, E. G. Kavousanaki, and I. E. Perakis, Phys. Rev. B **78**, 041301(R) (2008).

[12] R. A. Kaindl, D. Haegele, M. A. Carnahan, and D. S. Chemla, Phys. Rev. B **79**, 045320 (2009).

[13] D. Wang, M. Hawton, and M. M. Dignam, Phys. Rev. B **76**, 115311 (2007).

[14] F. Rossi and T. Kuhn, Rev. Mod. Phys. **74**, 895 (2002).

[15] H. Haug and S. W. Koch, *Quantum theory of optical and eletronic properties of semiconductors* (World Scientific, Singapore, 1990).

[16] V. M. Axt and A. Stahl, Z. Phys. B: Condens. Matter **93**, 195 (1994).

[17] E. Hanamura and H. Haug, Phys. Rep., Phys. Lett. **33**, 209 (1977).

[18] L. V. Butov, C. W. Lai, A. L. Ivanov, A. C. Gossard, and D. S. Chemla, Nature (London) **417**, 47 (2002).

[19] W. Hoyer, M. Kira, and S. W. Koch, Phys. Rev. B **67**, 155113 (2003).

[20] M. Kira and S. W. Koch, Eur. Phys. J. D **36**, 143 (2005).

[21] R. Takayama, N. H. Kwong, I. Rumyantsev, M. Kuwata-Gonokami, and R. Binder, Eur. Phys. J. B **25**, 445 (2002).

[22] Z. S. Yang, N. H. Kwong, R. Takayama, and R. Binder, Europhys. Lett. **69**, 417 (2005).

[23] D. Wang, Ph.D. thesis, Queen's University, 2008; URL: http://hdl.handle.net/1974/1593.

[24] M. M. Dignam and M. Hawton, Phys. Rev. B **67**, 035329 (2003).

[25] L. Yang, B. Rosam, J.-M. Lachaine, K. Leo, and M. M. Dignam, Phys. Rev. B **69**, 165310 (2004).

[26] Satoru Okumura and Tetsuo Ogawa, Phys. Rev. B **65**, 035105 (2001).

[27] C. Schindler and R. Zimmermann, Phys. Rev. B **78**, 045313 (2008).

[28] M. Combescot and O. Beebeder-Matibet, Europhys. Lett. **62**, 140 (2003).

[29] M. Hawton and D. Nelson, Phys. Rev. B **57**, 4000 (1998).

[30] V. Chernyak, W. M. Zhang, and S. Mukamel, J. Chem. Phys. **109**, 9587 (1998).

[31] D. Wang, A. Zhang, L. Yang, and M. M. Dignam, Phys. Rev. B **77**, 115307 (2008).

[32] K.-C. Je, M. Choi, S.-Y. Yim, J. S. Ahn, and S.-H. Park, Phys. Rev. B **66**, 155312 (2002).

[33] R. Huber, R. A. Kaindl, B. A. Schmid, and D. S. Chemla, Phys. Rev. B **72**, 161314(R) (2005).

[34] O. M. Schmitt, L. Bányai, and H. Haug, Phys. Rev. B **60**, 16506 (1999).

[35] M. M. Dignam and J. E. Sipe, Phys. Rev. Lett. **64**, 1797 (1990).

[36] M. M. Dignam and J. E. Sipe, Phys. Rev. B **43**, 4084 (1991).

[37] L. Yang, B. Rosam, and M. M. Dignam, Phys. Rev. B **72**, 115313 (2005).

[38] The computation using the full basis (the full simulation) is the most demanding one. We employ 60 processors (the processor used is UltraSPARC-IV+1.5 GHz) to deal with this computation. The computation of the XCs takes approximately 4 h and needs to be done only once. Solving the dynamic equations typically takes 33 h, which is reduced to around 20 h by removing the intraband coherence functions of HIESs with $m>4$ (see Sec. V A).

[39] There is a difference of a factor of 2 because the authors of Ref. 2 also consider the spin of the electron states, which in fact depends on the excitation condition.

[40] There is a difference of a factor of 4. One factor of 2 is from the consideration of spin, and depends on excitation conditions; it has the same origin as the factor 2 in the energy shift. The other factor of 2 is due to the square in Eq. (12), which is needed to obtain the oscillator strength.

[41] K.-H. Schlaad, C. Weber, J. Cunningham, C. V. Hoof, G. Borghs, G. Weimann, W. Schlapp, H. Nickel, and C. Klingshirn, Phys. Rev. B **43**, 4268 (1991).

[42] I. Bar-Joseph, T. K. Woodward, D. S. Chemla, D. Sivco, and A. Y. Cho, Phys. Rev. B **41**, 3264 (1990).

[43] V. Negoita, D. W. Snoke, and K. Eberl, Phys. Rev. B **61**, 2779 (2000).

[44] G. Tränkle, H. Leier, A. Forchel, H. Haug, C. Ell, and G. Weimann, Phys. Rev. Lett. **58**, 419 (1987).

[45] S. W. Koch, M. Kira, G. Khitrova, and H. M. Gibbs, Nat. Mater. **5**, 523 (2006).

[46] J.-M. Lachaine, Master's thesis, Lakehead University, 2002.